Nascent fragment shell effects on the nuclear fission processes in semiclassical periodic orbit theory

Ken-ichiro Arita,[1] Takatoshi Ichikawa,[2] and Kenichi Matsuyanagi[2,3]
[1]*Department of Physics, Nagoya Institute of Technology, Nagoya 466-8555, Japan*
[2]*Yukawa Institute for Theoretical Physics, Kyoto 606-8502, Japan*
[3]*Nishina Center, RIKEN, Wako 351-0198, Japan*

(Received 7 September 2018; published 10 December 2018)

Making use of the semiclassical periodic orbit theory (POT), we propose, for the first time, a method to exclusively evaluate the shell effects associated with each of the nascent fragments (prefragments) generated by the neck formation in nuclear fission processes. In spite of the strong indication of such shell effects in asymmetric fragment mass distributions, they could not have been accessed by any previous theoretical approach since most of the single-particle wave functions are delocalized. In the POT, we have found that the prefragment shell effects can be naturally and unambiguously identified as the contributions of the classical periodic orbits localized in each of the prefragments. For a numerical test, simple cavity potential models are employed with the shape described by the three-quadratic-surface shape parametrization. Deformed shell energies are studied with the trace formula for degenerate orbits in a truncated spherical cavity which was recently derived [K. Arita, preceding paper, Phys. Rev. C **98**, 064310 (2018)]. In this simple model, it is shown that the prefragment shell effect dominates the total shell energy shortly after the neck formation, and the magicity of the heavier prefragment plays a significant role in establishing the fission saddle with asymmetric shape which leads to an asymmetric scission.

DOI: 10.1103/PhysRevC.98.064311

I. INTRODUCTION

In low-energy fissions of actinide nuclei, observed fragment mass distributions show apparent asymmetry [1]. Since symmetric shapes are always favored in the liquid-drop model (LDM), the above asymmetry is attributed to the quantum shell effect. For fission of nuclei in the range of proton number $Z = 90$–100 and neutron number $N = 130$–150, distributions of the heavier fragments show distinctive concentrations at mass numbers around $A \approx 140$, which is close to the doubly magic nucleus ^{132}Sn. From this observation, shell effects of the fragments, which lower the binding energies of the final states, are considered to play an important role as the origin of the asymmetric fission. In the fission of lighter nuclei, fragment distributions are expected to be more symmetric because of the absence of such a strong shell effect. However, fissions of some neutron-deficient mercury isotopes have been revealed to be asymmetric in recent β-delayed fission experiments [2,3].

Several theoretical investigations have been done to understand the origin of these asymmetric fissions, e.g., with the shell correction method in five-dimensional deformation space [4,5] and with the fully microscopic constrained Hartree-Fock-Bogoliubov (HFB) method [6,7]. The interpretations of the origins of the asymmetry are somewhat different among those theoretical approaches, but the common recognition is that the shell effect in the process of fission, which is responsible for the positions of saddles in deformation space, plays an essential role in determining the fragment mass distribution.

The fissioning nucleus gets more elongated in one direction, and a neck is built which gradually separates the total system into two subsystems. Then, one may expect emergence of a kind of the shell effect associated with those nascent fragments. Following [8–10], we call such a nascent fragment a "prefragment" for brevity.

The effect of the prefragment shell structure was studied in the two-center shell model [11,12]. The effect could be seen immediately after getting over the second barrier of the potential where the prefragments are not yet well separated. In modern microscopic HFB calculations [6,7], it was found that the prefragment part of the density distribution is quite similar to that of the independent spherical magic nucleus. More recently, the spatial nucleon localization functions were investigated to study the prefragment formation in nuclear fission [9,13]. These theoretical results strongly indicate the existence of the prefragment shell effect, but the physical mechanisms for their appearance have not been understood well.

In this paper, we propose a simple way of extracting the prefragment shell effect, which originates from the spatially localized part of the mean-field potential constricted in the middle. Such shell effect could not have been evaluated in any previous theoretical approach due to the delocalization of the single-particle wave functions. Focusing on the fact that the semiclassical level density is expressed by a sum of contributions of the classical periodic orbits, we found that the prefragment shell effect can be naturally and unambiguously identified as contributions of the orbit confined in each of the prefragments. In Sec. II, after some remarks on the semiclassical theory of shell structure, the idea of extracting the prefragment shell effect in the fission process is presented by means of the periodic-orbit theory (POT). In Sec. III,

properties of the cavity potential model with three-quadratic-surfaces (TQS) parametrization is discussed. Semiclassical analysis of the TQS cavity model with the POT is presented in Sec. IV, and Sec. V is devoted to a summary and discussions.

II. SEMICLASSICAL FOUNDATION OF THE PREFRAGMENT SHELL EFFECT

A. Periodic orbit theory

In the semiclassical POT, the single-particle energy level density

$$g(e) = \sum_i \delta(e - e_i) \tag{1}$$

is represented as the sum over contributions of classical periodic orbits [14,15],

$$g(e) = \bar{g}(e) + \sum_\beta A_\beta(e) \sin\left[\frac{1}{\hbar} S_\beta(e) - \frac{\pi}{2}\mu_\beta\right]. \tag{2}$$

Here, $\bar{g}(e)$ represents the average level density, which is generally a smooth, monotonic function of e. The second term represents the oscillating part, and the sum is taken over all the classical periodic orbits. $S_\beta = \oint_\beta \boldsymbol{p}\cdot d\boldsymbol{r}$ is the action integral along the orbit β, μ_β is the Maslov index related to the number of caustic points along β, and the amplitude A_β is determined by the period, degeneracy, and stability of the orbit. This semiclassical expression (2) is known as the trace formula, and is derived by evaluating the trace of the transition amplitude represented in the path-integral form.

For the hard-wall potentials in which the action integral S_β is expressed as the product of the momentum $p = \hbar k$ and the orbit length L_β, one has

$$g(k) = g(e)\frac{de}{dk} = \bar{g}(k) + 2R_0 \sum_\beta (kR_0)^{D_\beta/2} A_\beta \times \sin\left(kL_\beta - \frac{\pi}{2}\mu_\beta\right). \tag{3}$$

R_0 is the length unit, which is taken here as the radius of a sphere having the same volume as the interior region of the cavity, which is assumed to be conserved. D_β is the degeneracy parameter for orbit β which forms a D_β-parameter family under the existence of a continuous symmetry.

Thus, the contribution of each orbit gives a regularly oscillating function of k. The scale of the oscillating structure is given by the variation δk, which causes the change of phase by 2π, namely,

$$L_\beta \delta k \simeq 2\pi, \quad \delta k \simeq \frac{2\pi}{L_\beta}. \tag{4}$$

This relation tells us that the gross shell effect (with large δk) is associated with the contributions of short orbits having small L_β. Amplitude is proportional to $k^{D_\beta/2}$ for a degenerate D_β-parameter family of orbits, and the families with higher degeneracies make more important contribution in the semiclassical limit. The dimensionless energy-independent amplitude factor A_β in Eq. (3) is related to the amplitude $A_\beta(e)$ in Eq. (2) by

$$A_\beta(e)\frac{de}{dk} = 2R_0(kR_0)^{D_\beta/2} A_\beta. \tag{5}$$

In the following, we use the symbol A_β for the dimensionless energy-independent amplitude, and the energy-dependent amplitude will be referred to explicitly with the argument when necessary.

The analytic expression of the trace formula for the spherical cavity was derived by Balian and Bloch [16]. The families of regular polygon orbits in the spherical cavity are classified by the two integers (p, t), where p is the number of vertices and t is the number of turns around the center. The length of the orbit (p, t) is given by

$$L_{pt} = R_0 l_{pt}, \quad l_{pt} = 2p\sin\varphi_{pt}, \quad \varphi_{pt} = \frac{t\pi}{p}, \tag{6}$$

where R_0 is the radius of the cavity. Polygon orbits ($p > 2t$) form three-parameter families ($D_{p>2t} = 3$) generated by the three-dimensional rotations, and diameter orbits ($p = 2t$) form two-parameter families ($D_{p=2t} = 2$) since the rotation about the orbit itself generates no family. The contribution of the family (p, t) to the semiclassical level density is given by

$$g_{pt}^{(\mathrm{sph})}(k) = 2R_0(kR_0)^{D_{pt}/2} A_{pt}^{(\mathrm{sph})} \sin\left(kL_{pt} - \frac{\pi}{2}\mu_{pt}^{(\mathrm{sph})}\right), \tag{7}$$

with the amplitude factor

$$A_{pt}^{(\mathrm{sph})} = \begin{cases} \sin 2\varphi_{pt}\sqrt{\frac{\sin\varphi_{pt}}{\pi p}} & (p > 2t), \\ \frac{1}{2\pi t} & (p = 2t) \end{cases} \tag{8}$$

and the Maslov index

$$\mu_{pt}^{(\mathrm{sph})} = \begin{cases} 2t - p - \frac{3}{2} & (p > 2t), \\ 2 & (p = 2t). \end{cases} \tag{9}$$

Using the formula (2) or (3), one can derive the trace formula for the shell energy,

$$\delta E(N) = \sum_\beta \frac{\hbar^2}{T_\beta^2} A_\beta(e_F) \sin\left[\frac{1}{\hbar} S_\beta(e_F) - \frac{\pi}{2}\mu_\beta\right] = \sum_\beta \frac{2\hbar^2 (k_F R_0)^{1+D_\beta/2}}{ML_\beta^2} A_\beta \sin\left(k_F L_\beta - \frac{\pi}{2}\mu_\beta\right), \tag{10}$$

where M is the particle mass and $e_F = (\hbar k_F)^2/2M$ is the Fermi level corresponding to the particle number N. Due to the extra factor proportional to $T_\beta^{-2} \propto L_\beta^{-2}$, relative contributions of the longer orbits are suppressed and only a few shortest orbits dominate the shell energies in general.

Supposing that a certain orbit β (isolated or degenerate) dominates in the periodic-orbit sum (10), namely,

$$\delta E(N) \approx \frac{\hbar^2}{T_\beta^2} A_\beta \sin\left[\frac{1}{\hbar} S_\beta(e_F) - \frac{\pi}{2}\mu_\beta\right], \tag{11}$$

the shell energy would take the minima at

$$S_\beta(e_F) = 2\pi\hbar\left(n + \frac{\mu_\beta - 1}{4}\right) \tag{12}$$

with integer n, and the corresponding particle number $N_n(e_F)$ gives the magic numbers for a given potential. When considering the shell structure as function of the deformation parameter δ, the formula

$$S_\beta(e_F,\delta) = 2\pi\hbar\left(n + \frac{\mu_\beta - 1}{4}\right) \tag{13}$$

gives the condition for the parameter δ to lower the deformation energy for particle number $N(e_F)$.

Strutinsky *et al.* have used the above constant-action lines (13) to explain the ridge-valley structure of the shell energy in the (δ, N) plane, where δ is the quadrupole deformation parameter [17]. Frisk discussed the origin of the deformed shell structures related to the prolate-oblate asymmetry in the spheroidal cavity model by means of constant-action-lines analyses [18]. It is also examined in the mean-field potential model with more general radial dependence [19].

Brack *et al.* considered the origin of the asymmetric fission with the POT [20]. They analyzed the deformed shell effect in the axially symmetric cavity potential model as function of the elongation parameter c and the asymmetry parameter α, and found that the fission path in the potential energy surface which connects the minimum at the symmetric shape and the strongly elongated asymmetric shape is simply explained by the constant-action line (13) for the shortest periodic orbit in the (c, α) plane, which is rewritten for the cavity model as

$$k_F L_\beta(c,\alpha) = 2\pi\left(n + \frac{\mu_\beta - 1}{4}\right). \tag{14}$$

In the following, we consider the origin of asymmetric fission through its relation to the prefragment shell effect. For this aim, we consider the way of extracting the contribution of spatially localized prefragment to the shell effect by using the POT.

B. Prefragment shell effect in the POT

Let us consider the deformation of a nucleus in a fission process where it gets elongated. In the LDM, one has competition between the surface energy and the Coulomb energy. With increasing elongation, the Coulomb effect surpasses the surface effect and the saddle is formed. The shell effect, namely, the quantum fluctuation, is superimposed on this saddle structure, which typically constructs a double-humped structure for nuclei in the actinide region. Since the Coulomb energy prefers a dumbbell shape rather than a rugby-ball shape, the neck is formed after getting over the saddle. One will expect that the prefragments would acquire identities and begin to affect the whole system after the formation of the neck. It is also expected that the above neck formation could be prompted by the quantum shell effect. However, in a purely quantum approach with the mean-field potential, it is usually impossible to extract the shell effect associated with the spatially localized part of the potential because most of the single-particle wave functions are delocalized.

Here, we pay attention to the fact that the neck formation gives birth to the classical periodic orbits confined in either of the prefragment parts, which we call the prefragment orbits. According to the spatial localization characteristics of the orbits, we decompose the trace formula (10) into three parts as

$$\delta E(N) = \delta E_1(N) + \delta E_2(N) + \delta E_3(N), \tag{15}$$

where δE_1 and δE_2 are contributions of the prefragment orbits in the first and second prefragments, respectively, and $\delta E_3(N)$ is the contribution of the other orbits traveling between the two prefragments or staying in the neck part. The contribution of the prefragment periodic orbits can be naturally identified as the shell effect associated with the prefragment part of the potential. This gives a simple and clear definition of the prefragment shell effect.

III. CAVITY MODEL WITH THE THREE-QUADRATIC-SURFACES PARAMETRIZATION

A. Shape parametrization for the fission process

Since our aim is to understand the role of the prefragments in the shell effect of fissioning nuclei, it is important to use a shape parametrization which allows flexible control of the prefragment deformations. The three-quadratic-surfaces (TQS) parametrization is one of the appropriate parametrizations for this purpose [21]. In this parametrization, two horizontally aligned ellipsoids are smoothly connected by the neck part, which is also given by a quadratic surface:

$$\rho^2(z) = \begin{cases} a_1^2 - \frac{a_1^2}{c_1^2}(z-l_1)^2 & (l_1 - a_1 \leqslant z \leqslant z_1), \\ a_2^2 - \frac{a_2^2}{c_2^2}(z-l_2)^2 & (z_2 \leqslant z \leqslant l_2 + a_2), \\ a_3^2 - \frac{a_3^2}{c_3^2}(z-l_3)^2 & (z_1 \leqslant z \leqslant z_2). \end{cases} \tag{16}$$

Among the eleven constants $\{a_{1-3}, c_{1-3}, l_{1-3}, z_{1,2}\}$, six are constrained by imposing the continuities of $\rho(z)$ and $\rho'(z)$ at the joints $z = z_1, z_2$, the center-of-mass condition and the volume-conservation condition. Thus, one eventually has five free parameters to determine the shape of the potential.

We use the set of parameters $\{\sigma_{1-3}, \alpha_{1-3}\}$ defined in [21] as

$$\begin{aligned} &\sigma_1 = \frac{l_2 - l_1}{u}, \quad \alpha_1 = \frac{l_1 + l_2}{2u} \quad \left(u = \sqrt{\frac{a_1^2 + a_2^2}{2}}\right), \\ &\sigma_2 = \frac{a_3^2}{c_3^2}, \quad \alpha_2 = \frac{a_1^2 - a_2^2}{u^2}, \\ &\sigma_3 = \frac{1}{2}\left(\frac{a_1^2}{c_1^2} + \frac{a_2^2}{c_2^2}\right), \quad \alpha_3 = \frac{a_1^2}{c_1^2} - \frac{a_2^2}{c_2^2}. \end{aligned} \tag{17}$$

σ_1 is proportional to the distance between the centers of the two prefragments and is regarded as the elongation parameter. σ_2 is proportional to the curvature of the middle surface and controls the shape of the neck. For the fission deformations, the neck surface is usually concave and σ_2 takes negative values. α_2 is related to the prefragment mass asymmetry. σ_3 and α_3 control the deformation of the two prefragments. The above five are taken as the free shape parameters. The

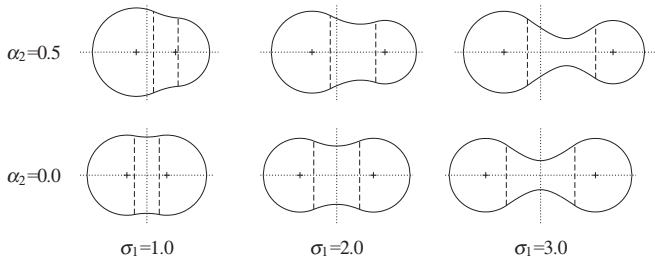

FIG. 1. The shapes of the potential surfaces in the TQS parametrization, varying the elongation parameter σ_1 and the prefragment mass asymmetry parameter α_2, with spherical prefragments ($\sigma_3 = 1$, $\alpha_3 = 0$) and fixed value of the neck parameter $\sigma_2 = -0.6$. The broken lines represent the joints of the neighboring quadratic surfaces, and the cross symbols represent the centers of the left and right prefragments. Horizontal and vertical dotted lines indicate the symmetry axis and the position of the center of mass, respectively.

parameter α_1 which describes the asymmetry of the centers of the prefragments is automatically determined by the above five parameters.

In this work, we fix the shapes of both prefragments to be spherical ($\sigma_3 = 1$, $\alpha_3 = 0$), and also fix the value of the neck parameter to a typical value $\sigma_2 = -0.6$, found in realistic calculations of the fission paths for U and Pu isotopes [5]. The radius of the jth prefragment ($j = 1, 2$) is denoted by R_j ($=a_j = c_j$) below. The shapes of the potential surface for several values of (σ_1, α_2) are displayed in Fig. 1.

Figure 2 shows the LDM deformation energies for the ^{236}U nucleus,

$$\Delta E_{\rm LDM} = (B_S - 1)a_S A^{2/3} + (B_C - 1)a_C \frac{Z^2}{A^{1/3}}, \qquad (18)$$

as functions of the elongation parameter σ_1 with some fixed values of the mass asymmetry parameter α_2. a_S (a_C) is the LDM surface (Coulomb) parameter for spherical nuclei, and B_S (B_C) is the deformation factor [22] (see the Appendix for B_S). One finds the saddle at $\sigma_1 \simeq 2.0$ for this nucleus, and also for nuclei in the actinide regions. For any given value of σ_1,

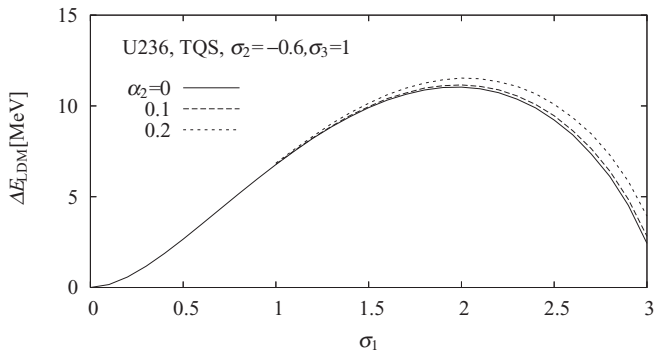

FIG. 2. Liquid-drop model deformation energies $\Delta E_{\rm LDM}$ for ^{236}U nucleus plotted as functions of the elongation parameter σ_1 with fixed values of the mass asymmetry parameter α_2. Solid, long-dashed and short-dashed lines represent the results for $\alpha_2 = 0$, 0.1 and 0.2, respectively.

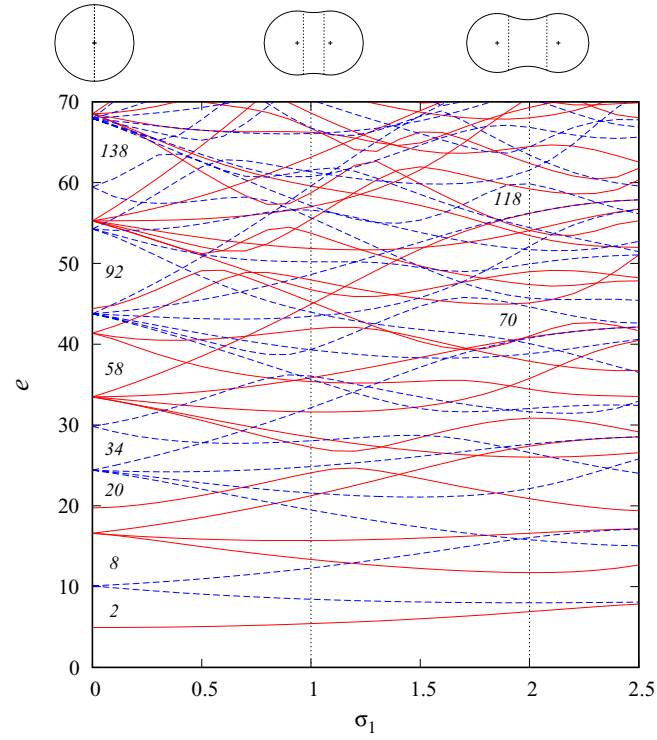

FIG. 3. Single-particle level diagram for the symmetric TQS cavity model as function of the elongation parameter σ_1. Solid (red) and broken (blue) lines represent the levels with positive and negative parities, respectively. The shapes of the potential surface at $\sigma_1 = 0$, 1.0, and 2.0 are shown at the top of the diagram.

the LDM energy takes the minimum at the symmetric shape, $\alpha_2 = 0$. Therefore, a trend to asymmetric shapes is considered to be purely a quantum effect in this TQS parametrization.

B. Single-particle spectra

The mean-field potential for a heavy nucleus is approximately flat near the center with depth of about 50 MeV, and sharply approaches zero around the surface with diffuseness of about 0.7 fm. The existence of strong spin-orbit coupling and pairing correlations is well known, but here we focus our attention on the roles of the shape evolution and adopt a simple infinite-well (cavity) potential model. The single-particle eigenvalue problem is solved by the spherical-wave decomposition method (SWDM) [23]. For the wave function expressed as the superposition of the spherical waves with given energy and K quantum number, one obtains the energy eigenvalue at which the boundary condition is satisfied extremely well.

Figure 3 shows the level diagram for a symmetric deformation. $\sigma_1 = 0$ corresponds to the spherical shape, and one sees shell closures for magic numbers $N = 2, 8, 20, 34, 58, 92, 138, \ldots$. Deformed shell closures are also found at large deformations, e.g., $N = 70, 118$ at $\sigma_1 \simeq 2$. One will also see some of the levels with different parities approaching each other at large σ_1, which may be related to localization of single-particle wave functions in each of the prefragments.

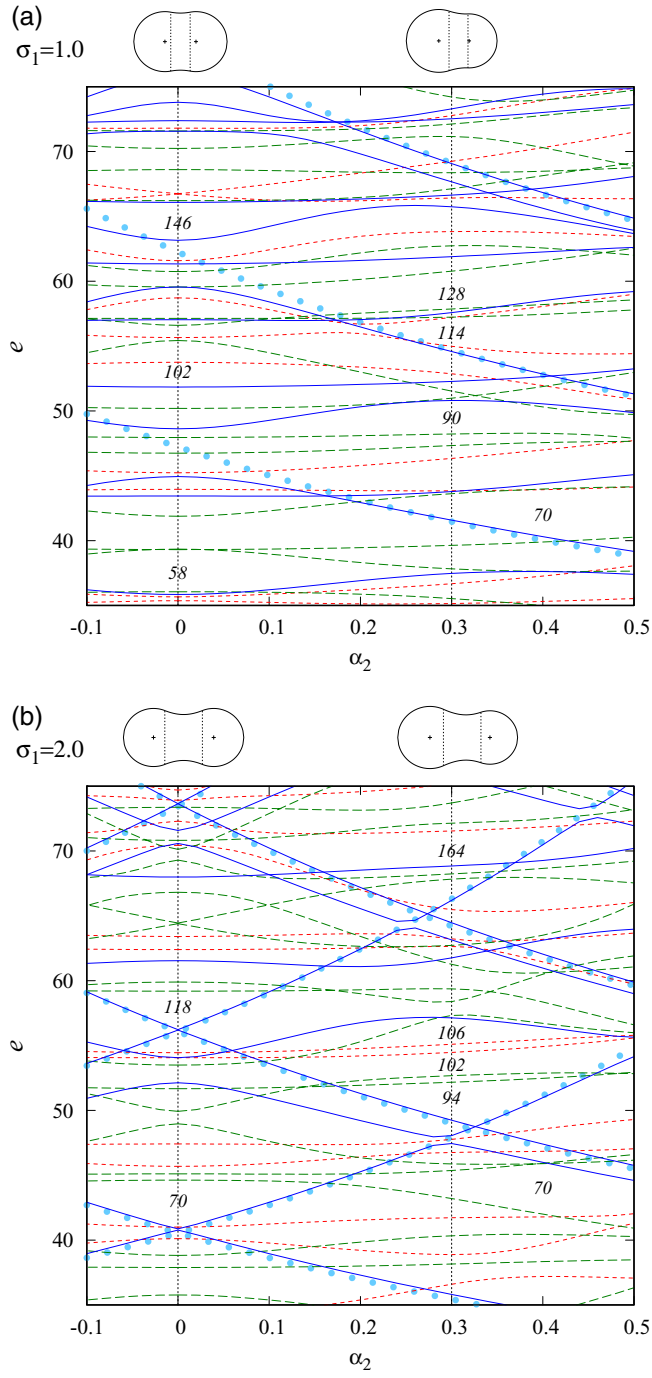

FIG. 4. Single-particle level diagrams as functions of the asymmetry parameter α_2, with the elongation parameter $\sigma_1 = 1.0$ (a) and 2.0 (b). The short-dashed (red), long-dashed (green), and solid (blue) lines represent levels with the magnetic quantum numbers $K = 0$, $1 \leqslant K \leqslant 2$, and $K \geqslant 3$, respectively. The thick dotted (light blue) lines are drawn so as to be proportional to $1/R_j^2$, which would be helpful for recognizing the levels indicating localization to each of the prefragments. Shapes of the surface at $\alpha_2 = 0$ and 0.3 are displayed at the top of each panel.

In Fig. 4, level diagrams as functions of the asymmetry parameter α_2 with fixed values of the elongation parameter σ_1 are shown. One finds significant differences between the diagrams for $\sigma_1 = 1.0$ and 2.0. For $\sigma_1 = 1.0$, most of the levels are nearly horizontal as functions of α_2 for small α_2, which indicates a chaotic nature. For large α_2, one sees some high-K levels going down with increasing α_2. Since their slopes are almost proportional to $1/R_1^2$, indicated by the thick dotted lines, they are considered to be the states localized in the heavier prefragments whose radius R_1 increases with α_2. In the diagram for $\sigma_1 = 2.0$ one sees both descending and ascending high-K levels with avoided crossings whose slopes are almost proportional to $1/R_1^2$ and $1/R_2^2$, respectively. Those levels indicate the appearance of the states localized in each of the prefragments due to the developed neck [24]. One finds several shell gaps showing up near the crossing points around $\alpha_2 \approx 0.3$.

The SWDM works sufficiently well for small elongation, but suddenly turns inaccurate for $\sigma_1 > 2.5$. We will have to find another method to look at the behavior of the level structure up to the scission point, which remains as a future problem.

C. Classical periodic orbits

In the TQS cavity model under consideration, classical periodic orbits are classified into the following four categories:

(i) prefragment polygon orbits in either of the spherical prefragments, which form three-parameter families;
(ii) prefragment diameter orbits in either of the spherical prefragments, which form two-parameter families;
(iii) meridian-plane orbits, equatorial orbits in the neck surface, and three-dimensional orbits, which form one-parameter families generated by the rotation about the symmetry axis;
(iv) an isolated straight-line orbit along the symmetry axis.

Figure 5 shows the lengths of some classical periodic orbits in a symmetric TQS cavity ($\alpha_2 = 0$) plotted as functions of the elongation parameter σ_1. Since the orbit with higher degeneracies play a dominant role for the shell effect, we might be able to consider the shell energy only with the contributions of the orbit families belonging to categories (i) and (ii), at least for sufficiently large σ_1. The prefragment orbit families in each of the spherical prefragments are labeled by the two indices (p, t) just as in an isolated spherical cavity discussed in Sec. II A. Polygon orbits $p > 2t$ belong to (i) and diameter orbits $p = 2t$ to (ii). The length of the orbit (p, t) in the jth prefragment ($j = 1, 2$) is given by

$$L_{j,pt} = R_j l_{pt}, \tag{19}$$

with l_{pt} defined by Eq. (6). For small elongation σ_1, prefragment orbits exist only in the narrow region around the planes $z = l_1$ and $z = l_2$, but the region broadens as the neck develops with increasing σ_1, and then their contributions to the level density will become more important. As we discussed in [25], the orbit families (i) and (ii) are accompanied by the marginal orbits having lower degeneracies than the principal family. Their contributions to the semiclassical level density should be treated separately from those of the principal families, and they play significant roles especially at small elongation.

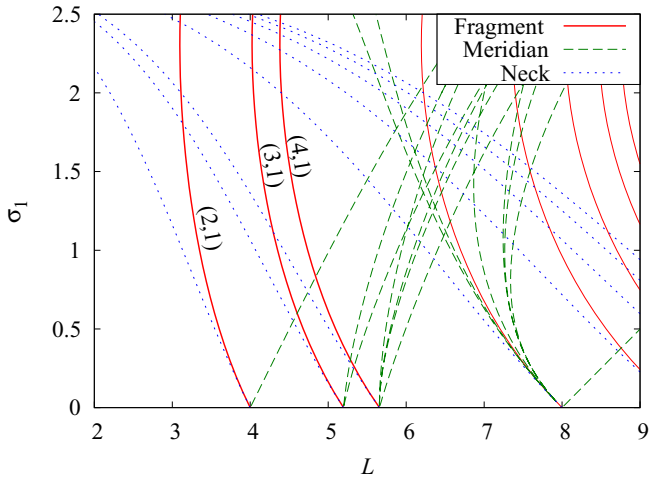

FIG. 5. Lengths of the symmetric classical periodic orbits in the TQS cavity model as functions of the elongation parameter σ_1, with spherical prefragments and the neck parameter fixed at $\sigma_2 = -0.6$. Solid lines (red) represent the prefragment orbits (p, t), broken lines (green) represent the meridian-plane orbits, and dotted lines (blue) represent the equatorial regular polygon orbits in the neck surface (see Ref. [25]).

IV. SEMICLASSICAL ANALYSIS OF THE PREFRAGMENT SHELL EFFECT

A. Fourier transforms of the level density

Thanks to the simple momentum dependence of the action integral, one can obtain clear correspondence between quantum shell structure and classical orbits through the Fourier transformation of the level density. Let us define the Fourier transform of the level density $g(k)$ with respect to the wave number k by

$$F(L) = \sqrt{\frac{2}{\pi}} \int_0^\infty dk\, g(k) e^{ikL} e^{-\frac{1}{2}(k/k_c)^2}. \tag{20}$$

The Gaussian in the integrand is introduced to truncate the high energy part ($k \gg k_c$) of the spectrum which is unavailable in the numerical calculations. The cutoff momentum k_c is taken as $k_c \approx k_{\max}/\sqrt{2}$, $k_{\max}$ being the value where the average density of numerical quantum levels begins to deviate from the (extended) Thomas-Fermi value. Inserting the quantum level density $g(k) = \sum_i \delta(k - k_i)$, one has

$$F^{\rm qm}(L) = \sqrt{\frac{2}{\pi}} \sum_{i=1}^{\infty} e^{ik_i L} e^{-\frac{1}{2}(k_i/k_c)^2}, \tag{21}$$

which can be easily calculated from the quantum spectrum. Inserting the semiclassical level density (3) into (20), one obtains

$$F^{\rm sc}(L) = F_0(L) + \sum_\beta (k_c R_0)^{1+D_\beta/2} A_\beta e^{-i\pi\mu_\beta/2} \times \Lambda_{D_\beta}\left(\frac{L - L_\beta}{\gamma}\right), \quad \gamma = k_c^{-1}, \tag{22}$$

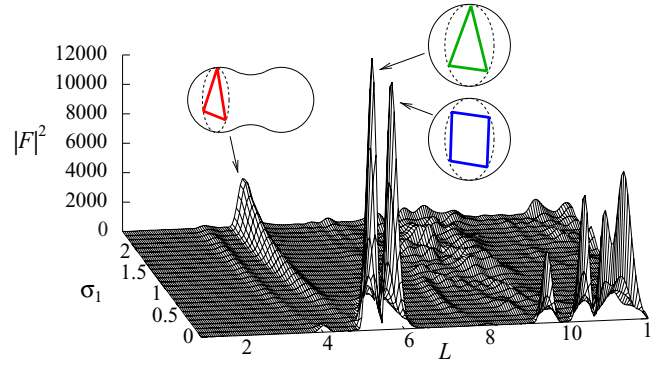

FIG. 6. Fourier transform of the single-particle level density. The squared amplitude $|F^{\rm qm}(L;\sigma_1)|^2$ is plotted as a function of L and the elongation parameter σ_1.

where $\Lambda_D(y)$ defined by

$$\Lambda_D(y) = \sqrt{\frac{2}{\pi}} \int_0^\infty dx\, x^{D/2} e^{ixy} e^{-x^2/2} \tag{23}$$

is the function having a single peak at $y = 0$ with height $|\Lambda_D(0)| \simeq 0.8$ and width $\Delta y \simeq 4$ for $D \geqslant 1$ [25]. Accordingly, (22) makes a function exhibiting peaks at the lengths of the orbits, $L = L_\beta$, with width $\Delta L \simeq 4\gamma$ and height $|F(L_\beta)| \propto A_\beta$. Thus, we can extract information on the periodic-orbit contributions out of the quantum spectrum by means of the above Fourier analysis.

Figure 6 shows the moduli of the Fourier transform (21) as function of σ_1 and L for symmetric deformation ($\alpha_2 = 0$). For the spherical shape ($\sigma_1 = 0$), one sees prominent peaks at the equilateral triangle orbit $L_{31} = 3\sqrt{3} \simeq 5.19$ (in units of R_0, which also applies below) and the square orbit $L_{41} = 4\sqrt{2} \simeq 5.65$. One also sees a small peak at the diameter orbit $L_{21} = 4$. The polygon orbits with more than five vertices have length close to that of the square orbit and their peaks are not resolved in this calculation. With increasing σ_1, the above two peaks promptly decay due to the breakdown of the spherical symmetry, but one can see the peak corresponding to the prefragment triangle family (3,1) growing for larger σ_1, as discussed in the previous section.

B. Shell energy

Taking account of the effect of marginal orbits, the contribution of the prefragment polygon orbit (p, t) in the jth prefragment ($j = 1, 2$) is expressed as

$$g_{j,pt}(k) = 2R_j \sum_{D=1}^{3} (kR_j)^{D/2} A_{j,pt}^{(D)} \sin\left(kL_{j,pt} - \frac{\pi}{2}\mu_{pt}^{(D)}\right) = 2R_j\, {\rm Im}[\mathcal{A}_{j,pt}(k) e^{ikL_{j,pt}}], \tag{24}$$

with the complex amplitude

$$\mathcal{A}_{j,pt}(k) = \sum_D (kR_j)^{D/2} A_{j,pt}^{(D)} e^{-i\pi\mu_{pt}^{(D)}/2}. \tag{25}$$

The summation is taken over the degeneracy parameter $1 \leqslant D \leqslant 3$. For the polygon orbit ($p > 2t$), the term for $D = 3$

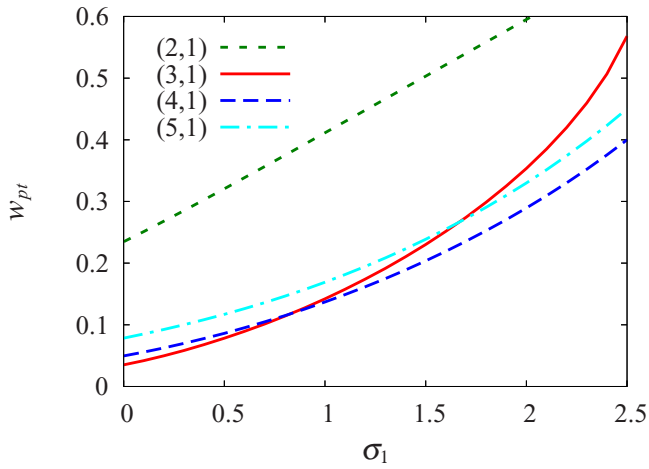

FIG. 7. The relative amplitude factors $w_{j,pt}$, given by Eq. (26), of some short prefragment orbit families (p,t) for symmetric shapes as functions of the elongation parameter σ_1. The wave number is put to the Fermi level $k = k_F$ corresponding to $N = 100$.

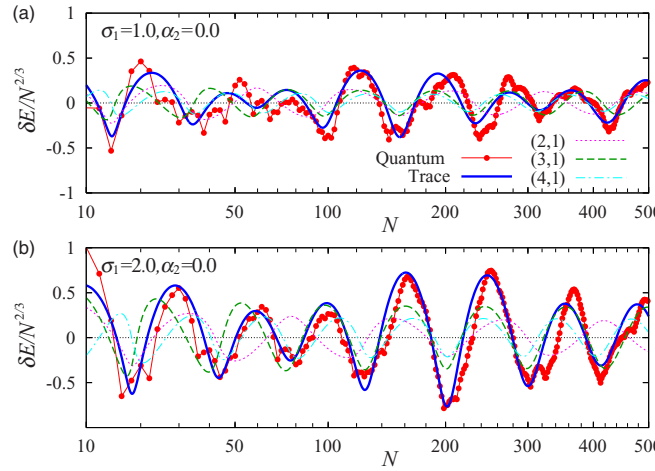

FIG. 8. Shell energies $\delta E(N)$ as functions of particle number N for symmetric shapes $\sigma_1 = 1.0$ (a) and 2.0 (b) with $\alpha_2 = 0$. The abscissa is taken to be linear in $N^{1/3}$, which also applies in the following Figs. 9–11. Thin solid lines with dots (red) represent the quantum results, and thick solid lines (blue) represent the results of the semiclassical trace formula with the contributions of the prefragment orbit families. The individual contributions of the diameter (2,1), triangle (3,1), and square (4,1) orbits are shown by the dotted (magenta), dashed (green), and dash-dotted (cyan) lines, respectively.

is the contribution of the principal three-parameter family which is given by a certain fraction of the formula for the spherical cavity. $D = 2$ is the contribution of the marginal orbits which have one vertex on the joint of the prefragment and neck surfaces. $D = 1$ is the contribution of the secondary marginal orbits which have two vertices on the joint. The last term is generally much smaller than the preceding two terms. For the diameter family ($p = 2t$), there is no $D = 3$ term and $D = 2$ is the contribution of the principal two-parameter family given by a certain fraction of that of the spherical cavity. $D = 1$ is the contribution of the marginal orbits. The analytic expressions for the amplitudes $A^{(D)}_{j,pt}$ and the Maslov indices $\mu^{(D)}_{pt}$ are given in Ref. [25].

Defining the amplitude relative to that for the entire spherical cavity,

$$w_{j,pt}(k) = \frac{|\mathcal{A}_{j,pt}(k)|}{(kR_j)^{D_{pt}/2} A^{(\mathrm{sph})}_{pt}}, \tag{26}$$

and the effective Maslov index $\mu^{(\mathrm{eff})}$ given through

$$-\frac{\pi}{2}\mu^{(\mathrm{eff})}_{j,pt}(k) = \arg \mathcal{A}_{j,pt}(k), \tag{27}$$

one can rewrite Eq. (24) as

$$g_{j,pt}(k) = 2R_j(kR_j)^{D_{pt}/2} w_{j,pt}(k) A^{(\mathrm{sph})}_{pt} \times \sin\left(kL_{j,pt} - \frac{\pi}{2}\mu^{(\mathrm{eff})}_{j,pt}\right), \tag{28}$$

and the contribution to the shell energy is expressed as

$$\delta E_{j,pt}(N) = \frac{2\hbar^2 (k_F R_j)^{1+D_{pt}/2}}{M L^2_{j,pt}} w_{j,pt} A^{(\mathrm{sph})}_{pt} \times \sin\left(k_F L_{j,pt} - \frac{\pi}{2}\mu^{(\mathrm{eff})}_{j,pt}\right). \tag{29}$$

Note that $w_{j,pt}$ and $\mu^{(\mathrm{eff})}_{j,pt}$ depend on the single-particle energy and are evaluated at the Fermi level. Figure 7 shows the relative amplitudes $w_{j,pt}$ at the Fermi level corresponding to $N = 100$ for several short-periodic-orbit families. At $\sigma_2 \simeq 2.0$ corresponding to the saddle of the LDM energy for actinide nuclei where the neck is expected to grow considerably, the value of w_{31} for the most important triangle orbit family amounts to 0.3–0.4, which means that the prefragment effect is more than 30% of the spherical shell effect, which is quite strong.

The value of w_{pt} for the diameter is considerably larger than those for polygons at small σ_1, which suggests that the relative contribution of the diameter family is more important in the truncated cavity than in the full spherical cavity. However, its absolute contribution is much less important than those of three-parametric polygon families due to the smaller degeneracy. Ignoring the contributions of orbits with smaller degeneracies $D_\beta < 2$, one can write the shell energy (15) only with the prefragment orbit family contributions,

$$\delta E_j(N) = \sum_{pt} \delta E_{j,pt}(N) \quad (j = 1, 2). \tag{30}$$

Figure 8 shows the semiclassical trace formula $\delta E(N) = \delta E_1(N) + \delta E_2(N)$ with Eqs. (30) and (29) for symmetric deformations, $\sigma_1 = 1.0$ and 2.0 with $\alpha_2 = 0$. Contributions of the prefragment orbit families $(p, 1)$ $(2 \leqslant p \leqslant 5)$ are taken into account. The orbit in either the first or the second prefragment gives the equivalent contribution for the symmetric shapes. One sees that the quantum results are nicely reproduced by our trace formula. In the figure, each contribution of (2,1), (3,1), and (4,1) orbits is also shown. One can see that the main oscillating structure is governed by (3,1), and the modulation of the shell structure, which is called a supershell structure, is provided due to the interference

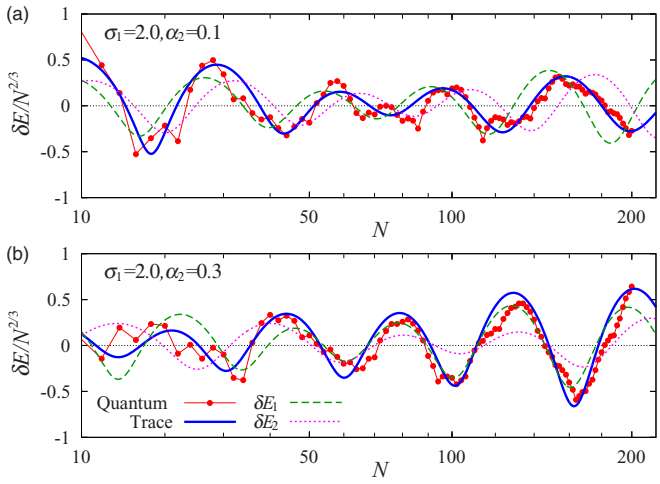

FIG. 9. Shell energies $\delta E(N)$ as functions of particle number N for asymmetric shapes $\alpha_2 = 0.1$ (a) and 0.3 (b) with fixed elongation parameter $\sigma_1 = 2.0$. The thin solid lines with dots (red) represent quantum results and the thick solid lines (blue) represent the results of semiclassical trace formula with contributions of the prefragment orbit families. The contributions of prefragment orbits in the first (heavy) and second (light) prefragments are shown by the dashed (green) lines and dotted (magenta) lines, respectively.

between different orbits. For instance, one sees deep energy minima for $N = 200$ where the three orbits (3,1), (4,1), and (2,1) make constructive contributions, while the minimum is shallower for $N = 80$ where the above contributions are somewhat destructive.

The results for asymmetric shapes, $\alpha_2 > 0$ with $\sigma_1 = 2.0$, are shown in Fig. 9, where the trace formula also succeeds in reproducing the quantum results. The contribution of each prefragment is also shown in this figure. Since the sizes of the two prefragments are different for asymmetric shapes, the same types of orbits but in different prefragments interfere with each other and bring about another supershell effect. For instance, in the panel for $\alpha_2 = 0.3$, the shell effect around $N \approx 160$ is much more enhanced than the other particle-number regions due to the constructive contributions of the two prefragments.

C. Shape asymmetry and the prefragment magicity

As we have shown above, the shell energy is dominated by the contributions of the prefragment orbit families. The main oscillating structure is governed by the triangle family (3,1). Looking at Fig. 7, one will also note that the relative amplitudes w_{pt} for the other polygon families take similar values through the change of σ_1. The Maslov indices for the marginal orbits are found to be given by $\mu^{(3)}_{pt} = \mu^{(2)}_{pt} + \frac{1}{2} = \mu^{(1)}_{pt} + 1$, and it may be allowed to approximate as $\mu^{(\mathrm{eff})}_{pt} \approx \mu^{(\mathrm{sph})}_{pt}$. Therefore, the prefragment shell effect should be similar to that of the independent spherical cavity. These suggest the possibility of expressing the shell energy of the total system containing the two spherical prefragments in terms of those for two spherical cavities.

By replacing $w_{j,pt}$ with $w_{j,31}$ and $\mu^{(\mathrm{eff})}_{j,pt}$ with $\mu^{(\mathrm{sph})}_{j,pt}$ in Eq. (29), one obtains the relation

$$\delta E^{(\mathrm{frag})}_j(N) \approx w_{j,31} \sum_{pt} A^{(\mathrm{sph})}_{pt} \sin\left(kL_{j,pt} - \frac{\pi}{2}\mu^{(\mathrm{sph})}_{j,pt}\right)$$
$$= w_{j,31}\delta E^{(\mathrm{sph})}(N_j; R_j). \tag{31}$$

N_j is the particle number for the spherical cavity with the radius R_j corresponding to the Fermi level k_F, which will be referred to as the particle number of the jth prefragment for convenience. Since the particle number of the spherical cavity of radius R is proportional to $(k_F R)^3$ in the lowest order (see Appendix), one has

$$N_j \approx \left(\frac{R_j}{R_0}\right)^3 N, \tag{32}$$

where R_0 is the radius of the total system in the spherical limit. In the above approximation (31), the diameter contribution causes the main error due to the difference between w_{21} and w_{31}, which may not be important for large N and will decrease for large σ_1. Consequently, the total shell energy can be approximately represented in terms of the shell energies of the two spherical cavities as

$$\delta E(N) \approx \sum_j w_{j,31}\delta E^{(\mathrm{sph})}(N_j; R_j), \tag{33}$$

which might be smoothly linked to the scission point where the shell energy is given by the sum of those for the two independent fragments. Assuming the existence of the dominant prefragment orbit, the above kind of relation is expected to hold in more generic mean-field models, and it tells us how the prefragment shell effect grows in a wide region of deformation from the second saddle to scission through the factor w, representing the contribution of the dominant prefragment orbit.

In Fig. 10, we show the shell energies evaluated using Eq. (33) for symmetric shapes and compare them with the exact ones. We found that the major pattern of the shell energy is nicely reproduced by the sum of the two shell energies of spherical cavities for $\sigma_1 \gtrsim 1.0$ with the coefficient w_{31} obtained by our formula. Most of the shell energy minima are explained by the prefragment magic numbers $N_j = 58, 92, 138$ as indicated in the figures. The values of the prefragment radius R_1 relative to the radius R_0 of the total system in the spherical limit and the corresponding prefragment particle number N_1 relative to the total particle number N are given in Table I for symmetric shapes with several values of σ_1. For small σ_1, two provisional prefragment spheres overlap and N_1/N is greater than 1/2. With increasing σ_1, N_1/N becomes smaller than 1/2, which suggests that the magicity of the prefragments contribute to the shell-energy minima at $N > 2N_1$. For instance, the $N \approx 200$ system has a deep energy minimum for symmetric deformation with $\sigma_1 = 2.0$ which is related to the prefragment magic number $N_1 = 92$. This kind of relation might be useful in considering the effect of the prefragment magic numbers on the fragment mass distribution.

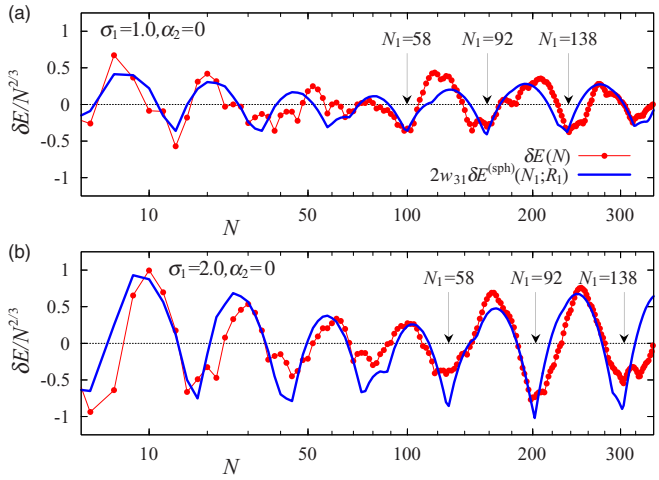

FIG. 10. Shell energies as functions of the particle number N for symmetric deformations ($\alpha_2 = 0$) with the elongation parameter $\sigma_1 = 1.0$ (a) and 2.0 (b). The thin line with dots (red) represents the quantum result and the thick line (blue) represents the prefragment shell effect $\delta E_{\rm frag}(N)$ which is approximately evaluated in terms of the shell energy of the spherical cavity as in Eq. (33). Arrows indicate the magic numbers of the spherical prefragments.

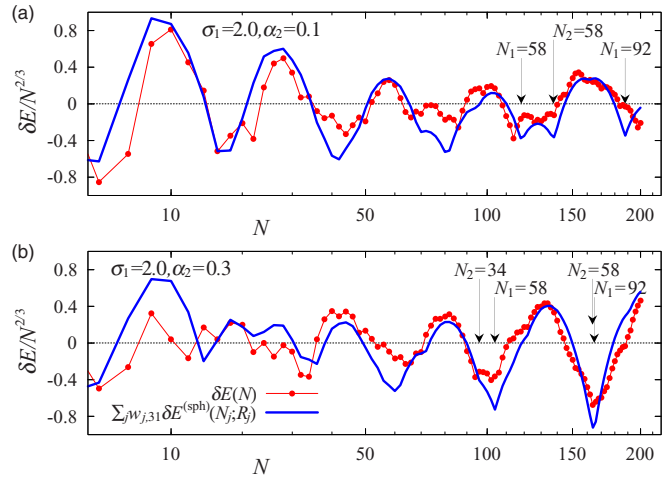

FIG. 11. Same as Fig. 10 but for asymmetric shapes. The mass asymmetry parameter is taken as $\alpha_2 = 0.1$ (a) and 0.3 (b), with the common elongation parameter $\sigma_1 = 2.0$.

In Fig. 11, we examine the relation (31) for asymmetric shapes with the elongation parameter fixed at $\sigma_1 = 2.0$. The radii R_j in units of R_0 and the prefragment particle numbers N_j relative to the total particle number N for several values of α_2 are listed in Table II. The exact shell energies are reproduced quite well by the approximation (31). One obtains especially large shell energy gains when the particle numbers of both prefragments coincide with the magic numbers, e.g., $N = 164$ for $\alpha_2 = 0.3$ where $N_1 = 92$ and $N_2 = 58$ are both spherical magic numbers. Since $N_1 + N_2$ is less than the total number of particles N, the rest of the particles which reside in the neck part will be distributed to the two fragments at the scission, and the fragments will have the particle numbers larger than N_j, supposing that the prefragment shapes are kept until scission. This is consistent with the experimental data for actinide nuclei where the heavier fragments in most cases have $A \simeq 140$, which is somewhat larger than that of the doubly-magic ^{132}Sn.

TABLE I. The prefragment radius $R_1 (= R_2)$ in units of R_0, and the prefragment particle number N_1 $(= N_2)$ relative to the total particle number N, used in evaluating the prefragment shell effect given by Eq. (33) for symmetric deformations ($\alpha_2 = 0$) at several values of the elongation parameter σ_1.

σ_1	R_1/R_0	N_1/N
0.5	0.90033	0.72980
1.0	0.83594	0.58414
1.5	0.79417	0.50089
2.0	0.76943	0.45552
2.5	0.75979	0.43861
3.0	0.76637	0.45011

For a fixed value of the elongation parameter σ_1, we calculated the shell energy $\delta E(N)$ as function of the asymmetry parameter α_2 and find the value of α_2 which minimizes the shell energy for each N. Then we evaluate the prefragment particle numbers N_j by Eq. (32) and plot them as functions of N in Fig. 12. Horizontal dotted lines indicate the spherical magic numbers. One sees that the particle number of the heavy fragment sticks to the magic numbers, which causes asymmetric minima for vast ranges of N. This behavior shows a nice correspondence with the fragment mass distribution in the fissions of actinide nuclei. One will notice that the feature can be found even for relatively small elongation $\sigma_1 = 1.0$. This suggests that the prefragment shell effect dominates the shell energy already at rather small elongation where the neck is not sufficiently developed. It would become effective with the development of neck formation after competition with the macroscopic energy, and would play an essential role in determining the shape of the fissioning nucleus.

D. Fission path and the constant-action line

In a situation where the shell effect is dominated by a certain periodic-orbit family β, the shell energy minima will appear along the constant-action lines (13), which are written as the constant-length lines (14) for the cavity system. As we

TABLE II. Radii R_j of the prefragments in units of R_0, and the prefragment particle numbers N_j relative to the total particle number N for several values of the mass asymmetry parameter α_2, with the elongation parameter $\sigma_1 = 2.0$.

α_2	R_1/R_0	N_1/N	R_2/R_0	N_2/N
0.1	0.78820	0.48986	0.74973	0.42142
0.2	0.80607	0.52373	0.72911	0.38760
0.3	0.82301	0.55747	0.70757	0.35425
0.4	0.83906	0.59071	0.68509	0.32154
0.5	0.85420	0.62327	0.66166	0.28967

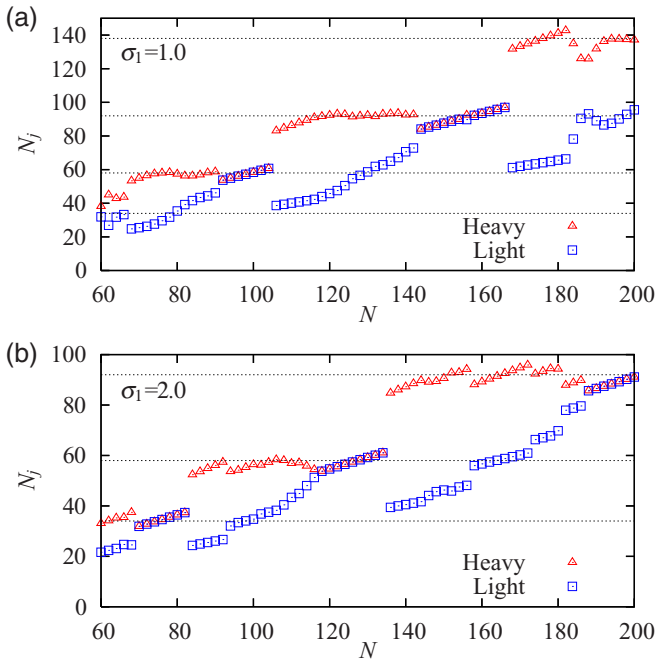

FIG. 12. Prefragment particle numbers N_1 (red triangle) and N_2 (blue square) for the mass asymmetry parameter α_2 which minimizes the shell energy for given total particle number N, with the elongation parameter $\sigma_1 = 1.0$ (a) and 2.0 (b). Horizontal dotted lines indicate the spherical magic numbers $N = \ldots, 34, 58, 92, 138, \ldots$.

see in the Fourier analysis, contributions of the prefragment triangle orbits play a dominant role in deformed shell effect in the TQS cavity model under consideration. Therefore, the shell energy minima are expected to arise along the constant-length lines of the triangle orbit given by

$$k_F(N)L_{j,31}(\sigma_1, \alpha_2) - \frac{\pi}{2}\mu_{31} = 2n\pi - \frac{\pi}{2} \tag{34}$$

with integer n; different magic numbers of the fragments correspond to the lines with different n. The Fermi level $k_F(N)$ is given by

$$k_F(N) \approx \frac{1}{R_0}\left\{\left(\frac{9\pi N}{4}\right)^{1/3} + \frac{3\pi B_S}{8}\right\}, \tag{35}$$

where B_S is the surface area relative to that of the sphere with the same volume (see Appendix).

In Fig. 13, contour plots of the shell energies $\delta E(N)$ are shown for several N as functions of deformation parameters σ_1 and α_2. Thick lines represent the constant-length lines of the prefragment triangle orbits in each of the two prefragments. One sees that the shell energy valleys appear along the constant-length lines and deep energy minima are located around the crossing points of the lines corresponding to the two prefragments.

For $N = 100$ and 164, one has symmetric minima around $\sigma_1 = 1$, that are connected with asymmetric minima around $(\sigma_1, \alpha_2) = (2, \pm 0.3)$ by the constant-length lines. Those lines are considered to represent the paths to asymmetric fissions. In fact, one finds that those lines nicely reproduce the behaviors of the fission paths obtained in more realistic calculations

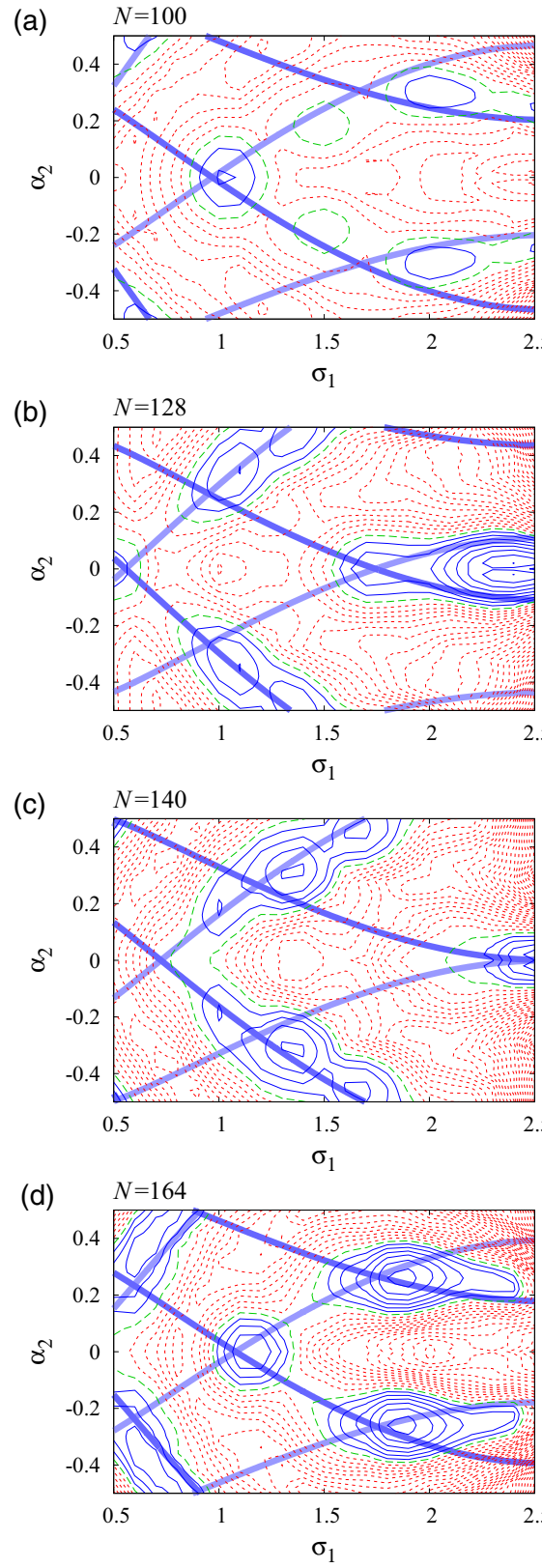

FIG. 13. Contour maps of the shell energy for several particle numbers on the deformation space (σ_1, α_2). Solid (blue) and dotted (red) contour lines represent negative and positive shell energies, respectively. Thick solid lines represent the constant-action lines (13) of the prefragment triangle orbits.

with the TQS parametrization [5]. The above feature is also consistent with what Brack *et al.* obtained in a different cavity model [20].

For $N = 128$ and 140, one has deep energy minima at symmetric shape with $\sigma_1 \gtrsim 2$ but they may not be reached from the normal-deformed minima around $\sigma_1 \approx 0.5$ due to the large potential barrier. The shape evolution would be strongly affected by the potential valley along the constant-length line toward asymmetric shapes, which leads to the asymmetric fission.

As shown in these calculations, the potential valleys are essentially determined by the prefragment magicity, and they have significant effect on the shape of the fissioning nucleus at saddles, that would be responsible for the fragment mass asymmetry.

V. SUMMARY

Semiclassical origin of the asymmetric fission is investigated with the idea of prefragment shell effects through the contribution of the periodic orbits confined in either of the prefragment parts of the potential. The cavity potential with the three-quadratic-surfaces (TQS) shape parametrization is employed to focus attention on the effect of the shape evolution. With the use of the trace formula, which was recently derived for a truncated spherical cavity, we have shown that the quantum shell energy is nicely reproduced in terms of the contributions of the prefragment periodic-orbit families. Taking notice of the fact that the triangle orbit family makes a dominant contribution to the shell effect, we have obtained a relation which expresses the deformed shell energy of the TQS cavity in terms of those of the isolated spherical fragments. This relation clarifies the roles of the prefragment magicity in formation of the fission path in the potential energy surface.

In a more realistic mean-field potential with finite diffuseness and spin-orbit coupling, the triangle-type orbit plays a dominant role in emergence of the distinct spherical magic numbers [26]. This suggests that a relation like (31) might be accessible also in the more general realistic mean-field models.

The prefragment shapes are assumed to be spherical in the present study, but the effects of the prefragment deformations should be taken into account in general. In the realistic macroscopic-microscopic model analysis using the TQS parametrization, consideration of the full five-dimensional potential energy surface is crucial in obtaining the correct fission saddles to reproduce the experimental results [5]. (To be more precise, the competitive effects by macroscopic and shell parts are also found to be significant in many situations.) Recently, importance of the octupole degrees of freedom for the prefragment shape has been suggested [27]. We expect that the POT analysis is useful in investigating the stability of the prefragment shape, which is among the key ingredients in describing the fission dynamics. Emergence of the remarkable shell structure at a certain deformation is often related to the local symmetry restoration caused by the periodic-orbit bifurcation [28], around which the amplitude of the trace formula takes a significant enhancement [26].

APPENDIX: WEYL FORMULA FOR THE AVERAGE LEVEL DENSITY

For a particle with mass M confined in a three-dimensional infinite-well potential, average level density is given by the Weyl asymptotic expansion formula [29]

$$\bar{g}(e) = \frac{2M}{\hbar^2}\left(\frac{kV}{4\pi^2} - \frac{S}{16\pi} + \frac{K}{12\pi^2 k}\right). \tag{A1}$$

Here, k stands for the wave number $k = \sqrt{2Me}/\hbar$, V and S are volume and surface area of the potential well, and K is the surface integral of the mean curvature,

$$K = \oint dS \frac{1}{2}\left(\frac{1}{R_1} + \frac{1}{R_2}\right), \tag{A2}$$

with R_1 and R_2 being the main curvature radii. For an axially symmetric surface $\rho = \rho_s(z)$ $(z_{\min} \leqslant z \leqslant z_{\max})$ with fixed volume $V = 4\pi R_0^3/3$, one has

$$\bar{g}(e) = \frac{2MR_0^2}{\hbar^2}\left(\frac{kR_0}{3\pi} - \frac{B_S}{4} + \frac{B_K}{3\pi kR_0}\right), \tag{A3}$$

where B_S and B_K are the surface area and the surface integral of the mean curvature relative to those for spherical shape,

$$B_S = \frac{1}{2R_0^2}\int_{z_{\min}}^{z_{\max}} \rho_s \sqrt{1 + (d\rho_s/dz)^2}\, dz, \tag{A4}$$

$$B_K = \frac{1}{4R_0}\int_{z_{\min}}^{z_{\max}} \left\{1 - \frac{\rho_s(d^2\rho_s/dz^2)}{1 + (d\rho_s/dz)^2}\right\} dz. \tag{A5}$$

Using the wave number variable k, one has

$$\bar{g}(k) = 2R_0\left\{\frac{(kR_0)^2}{3\pi} - \frac{B_S kR_0}{4} + \frac{B_K}{3\pi}\right\}. \tag{A6}$$

The average particle number filled up to the Fermi level $k = k_F$, taking account of the spin degeneracy factor, is given by

$$\begin{aligned}\bar{N}(k_F) &= 2\int_0^{k_F} \bar{g}(k)dk \\ &= \frac{4(k_F R_0)^3}{9\pi} - \frac{B_S(k_F R_0)^2}{2} + \frac{4B_K k_F R_0}{3\pi},\end{aligned} \tag{A7}$$

which is inverted as

$$k_F(N) \approx \frac{1}{R_0}\left\{\left(\frac{9\pi N}{4}\right)^{1/3} + \frac{3\pi B_S}{8}\right\} + \mathcal{O}(N^{-1/3}). \tag{A8}$$

[1] A. N. Andreyev, K. Nishio, and K.-H. Schmidt, Rep. Prog. Phys. **81**, 016301 (2018).
[2] A. N. Andreyev *et al.*, Phys. Rev. Lett. **105**, 252502 (2010).
[3] E. Prasad, D. J. Hinde, K. Ramachandran, E. Williams, M. Dasgupta, I. P. Carter, K. J. Cook, D. Y. Jeung, D. H. Luong, S. McNeil, C. S. Palshetkar, D. C. Rafferty, C. Simenel,

A. Wakhle, J. Khuyagbaatar, C. E. Düllmann, B. Lommel, and B. Kindler, Phys. Rev. C **91**, 064605 (2015).
[4] P. Möller, J. Randrup, and A. J. Sierk, Phys. Rev. C **85**, 024306 (2012).
[5] T. Ichikawa, A. Iwamoto, P. Möller, and A. J. Sierk, Phys. Rev. C **86**, 024610 (2012).
[6] M. Warda, A. Staszczak, and W. Nazarewicz, Phys. Rev. C **86**, 024601 (2012).
[7] J. D. McDonnell, W. Nazarewicz, and J. A. Sheikh, Phys. Rev. C **87**, 054327 (2013).
[8] N. Schunck and L. M. Robledo, Rep. Prog. Phys. **79**, 116301 (2016).
[9] J. Sadhukhan, C. Zhang, W. Nazarewicz, and N. Schunck, Phys. Rev. C **96**, 061301(R) (2017).
[10] K.-H. Schmidt and B. Jurado, Rep. Prog. Phys. **81**, 106301 (2018).
[11] U. Mosel and H. W. Schmitt, Nucl. Phys. A **165**, 73 (1971).
[12] U. Mosel and H. W. Schmitt, Phys. Rev. C **4**, 2185 (1971).
[13] C. L. Zhang, B. Schuetrumpf, and W. Nazarewicz, Phys. Rev. C **94**, 064323 (2016).
[14] M. C. Gutzwiller, J. Math. Phys. **12**, 343 (1971).
[15] M. Brack and R. K. Bhaduri, *Semiclassical Physics* (Westview, Boulder, CO, 2003).
[16] R. Balian and C. Bloch, Ann. Phys. (N.Y.) **69**, 76 (1972).
[17] V. M. Strutinsky and A. G. Magner, Sov. J. Part. Nucl. **7**, 138 (1976).
[18] H. Frisk, Nucl. Phys. A **511**, 309 (1990).
[19] K. Arita, Phys. Rev. C **86**, 034317 (2012).
[20] M. Brack, S. M. Reimann, and M. Sieber, Phys. Rev. Lett. **79**, 1817 (1997).
[21] J. R. Nix, Nucl. Phys. A **130**, 241 (1969).
[22] P. Ring and P. Schuck, *The Nuclear Many-Body Problem*, (Springer-Verlag, New York, 1980).
[23] T. Mukhopadhyay and S. Pal, Nucl. Phys. A **592**, 291 (1995).
[24] M. Brack, M. Sieber, and S. M. Reimann, Phys. Scr. T **90**, 146 (2001).
[25] K. Arita, preceding paper, Phys. Rev. C **98**, 064310 (2018).
[26] K. Arita, Phys. Scr. **91**, 063002 (2016).
[27] G. Scamps and C. Simenel, arXiv:1804.03337.
[28] A. Sugita, K. Arita, and K. Matsuyanagi, Prog. Theor. Phys. **100**, 597 (1998).
[29] R. Balian and C. Bloch, Ann. Phys. (N.Y.) **60**, 401 (1970).